RSC Advances

ROYAL SOCIETY OF CHEMISTRY

www.rsc.org/advances

Cite this: DOI: 10.1039/c0xx00000x

www.rsc.org/xxxxxx

ARTICLE TYPE

One-pot low-temperature synthesis of $MnFe_2O_4$-graphene composite for lithium ion battery application

Huang Tang,[a,b] Peibo Gao,[a] An Xing,[a] Shuang Tian,[a] and Zhihao Bao[a*]

Received (in XXX, XXX) Xth XXXXXXXXX 20XX, Accepted Xth XXXXXXXXX 20XX

DOI: 10.1039/b000000x

$MnFe_2O_4$-reduced graphene oxide (rGO) nanocomposite was successfully synthesized with a one-pot low-temperature process by coprecipitation of Mn ions produced in the modified Hummer's method and in situ reduction of GO at 90 °C. It exhibited excellent electrochemical performance, retaining a reversible capacity of 581.2 mAh g^{-1}, about 70% of the theoretical capacity, at a specific current of 1 A g^{-1} after 200 cycles.

Introduction

Nowadays, high-capacity anode materials with high safety and environmental friendliness are being sought to improve power and energy density of lithium ion batteries (LIBs), a promising power source for practical applications in the hybrid electric vehicles. [1] Graphite is the most common anode material for the commercial rechargeable LIBs for many years. However, its low reversible storage capacity cannot meet the growing demands for the high-capacity LIBs.[2] On the other hand, transitional metal-oxide nanomaterials, such as FeO, NiO, CoO_x, TiO_2, $ZnMn_2O_4$ and so on,[3] have been investigated as anode materials for LIBs owning to their higher specific capacities than graphite. However, the metal oxides have poor conductivity and suffer from volume change due to Li intercalation/extraction during the discharge/charge process,[4] which may lead to irreversible capacity loss and poor cycling stability. Meanwhile, graphene has emerged as a promising anode material due to its good chemical stability, excellent electronic conductivity, large specific surface area, and good structural flexibility.[5] But the large irreversible capacity, low initial Coulombic efficiency and fast capacity fading make it not suitable as high-performance anode for LIBs.[6] To take their advantages as anode materials, transitional metal-oxide nanomaterials (*e.g.* MnO_x, FeO_x, SnO_x, TiO_x, and VO_x) and graphene were combined as nanocomposites,[5,7-12] which exhibited good rate capability and cycling stability. In the synthesis of most of above nanocomposites, graphene oxide (GO) was used as a precursor of graphene. However, separation and purification of GO required tremendous work. Additionally, large amount of waste water containing Mn ions was produced especially when the Hummer's or modified Hummer's method was used to synthesize GO.[13]

To simplify synthesis of graphene nanocomposite and alleviate the environment pollution in the synthesis, a one-pot process was developed to obtain $MnFe_2O_4$-rGO nanocomposite in this study. In the process, we reduced the Mn ions produced in the synthesis of graphene oxide with modified Hummer's method to supply Mn^{2+} ions. Then, the mixture containing Mn^{2+} and graphene oxide was coprecipitated at mild temperature (e. g., 90 °C) to form $MnFe_2O_4$-graphene nanocomposite by adding Fe^{3+} and the reducing agent. To our knowledge, it was the first time to report a process which could directly convert the mixture produced with modified Hummer's method into metal-oxide and graphene nanocomposite.The lithium storage ability of the nanocomposite was also investigated. At a specific current of 1 A g^{-1}, the $MnFe_2O_4$-rGO electrode could still remain a capacity of 581.2 mAh g^{-1}, about 70% of theoretical capacity after 200 discharge/charge cycles.

Experimental section

Synthesis of GO

GO was prepared with a modified Hummer's method.[13a, 14] Briefly, powdered flake graphite (1.0 g, 500 mesh) and $NaNO_3$ (0.75 g) were placed in a flask. H_2SO_4 (75.0 ml, 98 wt%) was then added with mechanical stirring in an ice-water bath. After 10 min, $KMnO_4$ (4.5 g) was added gradually in the flask in 1 h. Then the mixture was stirred vigorously until it became pasty brownish at room temperature, and then diluted with deionized water. H_2O_2 aqueous solution (20 ml, 30 wt%) was then slowly added into the mixture to ensure that the rest high-valence manganese ions in the mixture were reduced into Mn^{2+} .

Synthesis of $MnFe_2O_4$-rGO

The mixture containing GO was ultrasonicated for 2 h, and then diluted to 3000 ml with deionized water. $FeCl_3$ (9.237 g) was dissolved in 400 ml deionized water, and then added into the diluted GO solution. The residual hydrogen peroxide in the solution was allowed to be decomposed into water and oxygen by ferric chloride as a catalyst. Ammonia aqueous solution (30 wt%) was added to adjust its pH to 10 in 2 h. The temperature of solution was raised to 90 °C and 30 ml of hydrazine hydrate (98 wt %) was added slowly with constant stirring, resulting in a black suspension. After being rapidly stirred for 4 h, the black suspension was cooled to room temperature, and then suspended solids were separated with magnets, washed with deionized water and ethanol several times, and finally dried in vacuum at 60 °C.

Synthesis of $MnFe_2O_4$.

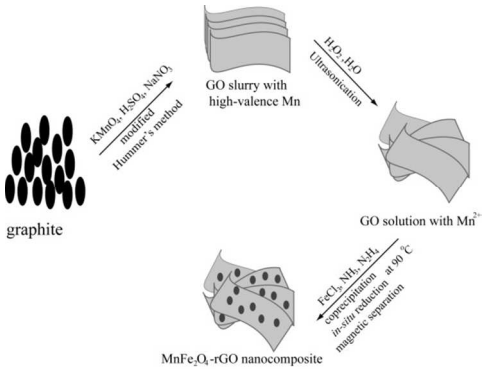

Figure 1. Schematic of synthesis of the $MnFe_2O_4$-rGO nanocomposite.

$MnFe_2O_4$ nanocrystals were prepared by a low-temperature coprecipitation method. $MnCl_2{\cdot}4H_2O$ (0.990 g) and $FeCl_3$ (1.622 g) were first dissolved in 300 ml deionized water with mechanical stirring at room temperature. Ammonia aqueous solution (30 wt%) was added to this solution to adjust its pH to 10. The temperature of solution was then raised to 90 °C with an oil bath, and the solution was rapidly stirred for 4 h, resulting in brownish black solution. After the brownish black solution was cooled to room temperature, the suspended solids were separated with a magnet, washed with deionized water and ethanol several times, and finally dried in vacuum at 60 °C.

Characterizations

X-ray diffraction (XRD) patterns were obtained by a diffractometer (Bruker D8 Discover) with Cu Kα radiation (λ = 1.5418 Å, 40 kV, 40 mA). The morphology of samples was observed by a high-resolution transmission electron microscopy (HRTEM, JEOL 2100F). The rGO content in the $MnFe_2O_4$-rGO composite was determined by a thermogravimeter (NETZSCH STA 449C) and the measurements were carried out in air in a range of 25-800 °C with a ramp rate of 10 °C /min. The N_2 absorption-desorption analysis was conducted at 77 K on a TriStar 3000. Raman spectra were measured on a Labram HR800 spectrometer.

Electrochemical measurement

The powder of $MnFe_2O_4$ and $MnFe_2O_4$-rGO as active materials, Super P carbon black and polyvinyldifluoride (weight ratio 80:10:10) were mixed in N-Methylpyrrolidone (NMP) solvent to produce a slurry. The slurry was coated onto a copper foil using the doctor-blading method and then dried to form the working electrode. The electrochemical tests were performed using two-electrode coin-type cells (CR 2016) with lithium as the counter electrode. One molar solution of $LiPF_6$ in a 1:1:1 (volume ratio) mixture of ethylene carbonate (EC), diethyl carbonate (DEC) and dimethyl carbonate (DMC) was used as the electrolyte. Cell assembling was carried out in an argon-filled glove box. Galvanostatic charge–discharge cycling was conducted using a battery tester (Land2100A) with a voltage window of 0.01-3 V at various current densities. All galvanostatic charge–discharge cycling tests were performed at 25 °C. Electrochemical impedance spectroscopy (EIS) measurement was carried out by using Autolab 302N electrochemical workstation (5 mV, 100 kHz-0.01 Hz).

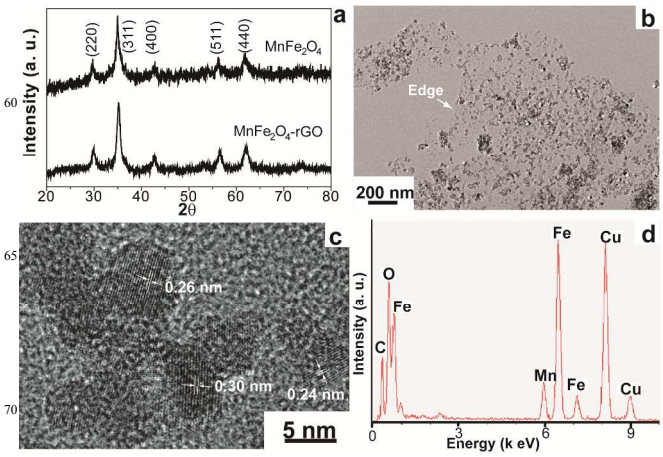

Figure 2. Characterization of the $MnFe_2O_4$-rGO nanocomposite: (a) XRD patterns of the nanocomposite and bare $MnFe_2O_4$ particles. TEM image (b), HRTEM image(c) and EDX analysis (d) of $MnFe_2O_4$-rGO nanocomposite.

Results and discussion

The one-pot process for synthesis of $MnFe_2O_4$-rGO nanocomposite was illustrated in Fig. 1. In the process, a slurry containing GO was prepared by a modified Hummer's method. Then high-valence manganese ions contained in the slurry were reduced to the low-valence Mn^{2+} by adding enough H_2O_2 aqueous solution. The slurry was then diluted into suspension by adding water. Mn^{2+} ions in the suspension were coprecipitated with Fe^{3+} in an alkaline environment to form $MnFe_2O_4$ nanocrystals, which nucleated and grew on GO nanosheets. At the same time, GO was reduced to graphene with the appearance of N_2H_4 at 90 °C. The X-ray diffraction patterns of $MnFe_2O_4$ and the $MnFe_2O_4$-rGO nanocomposite were shown in Fig. 2a. All diffraction peaks could be readily indexed to the cubic $MnFe_2O_4$ (JCPDS card No. 10-319). rGO peak in the XRD pattern of $MnFe_2O_4$-rGO did not appear, which suggested that $MnFe_2O_4$ nanoparticles could act as spacer to keep rGO layers separated and form disordered structure.[15] The crystallite size of $MnFe_2O_4$ in the nanocomposite was calculated to be 10.0 nm based on Scherrer analysis of the pattern. While the $MnFe_2O_4$ nanocrystals synthesized under the same condition without GO had a smaller crystallite size (6.5 nm). The difference in the crystallite size was due to the homogenous nucleation of $MnFe_2O_4$ nanocrystals for the latter one. TEM images of the nanocomposite (Fig. 2b) showed that graphene nanosheets extended themselves very well and were unagglomerated. $MnFe_2O_4$ nanoparticles with a size of several nanometers were decorated on the nanosheets. Such morphology might benefit from their synthesis process. In the process, GO precursor kept unagglomerated since no drying process was needed for its preparation and low-temperature synthesis could limit the growth of $MnFe_2O_4$ nanoparticles. The structure of synthesized nanocomposite could effectively prevent the aggregation of $MnFe_2O_4$ nanoparticles and the restacking of rGO sheets to ensure relatively large active specific surface area (69.53 m^2 g^{-1}, Fig. S1).[16] HRTEM images (Fig. 2c) of the nanocomposite further showed the clear lattice fringes with interplanar distances of 0.25, 0.26, 0.30 nm, corresponding to

(222), (311), and (220) planes of cubic $MnFe_2O_4$ crystal, respectively. The compositions of the

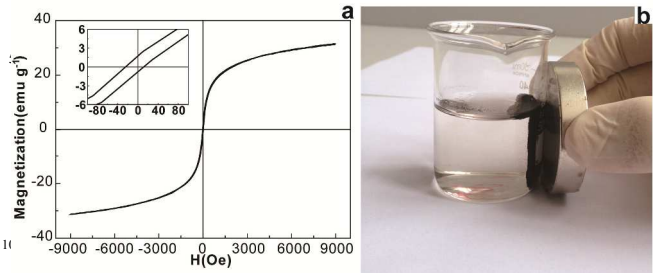

Figure 3. Magnetic property of the $MnFe_2O_4$-rGO nanocomposite: (a) Hysteresis curve of the $MnFe_2O_4$-rGO nanocomposite (inset, close view of hysteresis loops) and (b) magnetic separation of the $MnFe_2O_4$-rGO nanocomposite.

nanocomposite were further confirmed by Raman spectra (Fig. S2). In the spectra, the peak at 600 cm^{-1} corresponded to the vibration of $MnFe_2O_4$ while the other two dominant peaks at 1325 and 1600 cm^{-1} were attributed to D and G bands of rGO, respectively.[9, 17] The weight ratios of rGO sheets and $MnFe_2O_4$ components in the $MnFe_2O_4$-rGO nanocomposite were evaluated to be approximately 20% and 80%, by thermal gravimetric analysis (TGA, Fig. S3) in air, respectively. Above results indicated $MnFe_2O_4$-rGO nanocomposite was successfully synthesized. Table S1 summarized the synthesis processes of the transitional metal oxide-grapehene in the similar work. It revealed that the synthesis process in this work is more facile, economical and time-efficient than in other similar work. Fig. 3 showed the hysteresis loop of the nanocomposite measured at room temperature (300 K) by a Vibrating Sample Magnetometer (LakeShore 7407). The saturation magnetization was 31.4 emu g^{-1}, which was much smaller than the 80.0 emu g^{-1}, the saturation magnetization of bulk $MnFe_2O_4$.[18] The remnant magnetization and coercivity of nanocomposite were 1.25 emu g^{-1} and 18.68 Oe, respectively. The reduction in the value of saturation magnetization, remnant magnetization and coercivity could be attributed to formation of superparamagnetic state due to the size effect. The relationship between the particle size (d) and the saturation magnetization (σ_s) followed as:[18]

$$\sigma_s = \sigma_s(bulk)\left(1-\frac{6t}{d}\right)$$

where, $\sigma_s(bulk)$ is the magnetization of bulk $MnFe_2O_4$, 80.0 emu g^{-1} at 300 K and t is the thickness of the dead layer, 0.6 nm. Based on the above formula, the average crystallite size of the composite was calculated to be 7.5 nm, which approached the calculated crystallite size of $MnFe_2O_4$ based on the XRD pattern. Such superparamagnetic state with small remnant magnetization and coercivity at room temperature could allow the nanocomposite to be readily attracted and extracted by even a small external magnetic field. In fact, a magnet could easily separate the nanocomposite from the water suspension (Fig. 3b), which made the separation of nanocomposite easy and simplify the whole synthesis process.

The lithium-storage properties of the as-prepared $MnFe_2O_4$-rGO nanocomposite as an anode material for LIBs were studied. Representative galvanostatic charge–discharge profiles of the $MnFe_2O_4$-rGO nanocomposite at various specific current densities were shown in Fig. 4a. At 50 mA g^{-1}, the $MnFe_2O_4$-rGO electrode

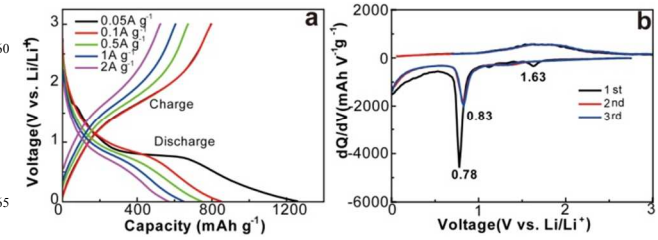

Figure 4. (a) Representative voltage profiles of $MnFe_2O_4$-rGO at various current densities and (b) plots of the differential capacity (dQ/dV) vs. voltage (V) for the first three cycles).The electrode surface area was 1.1 cm^2.

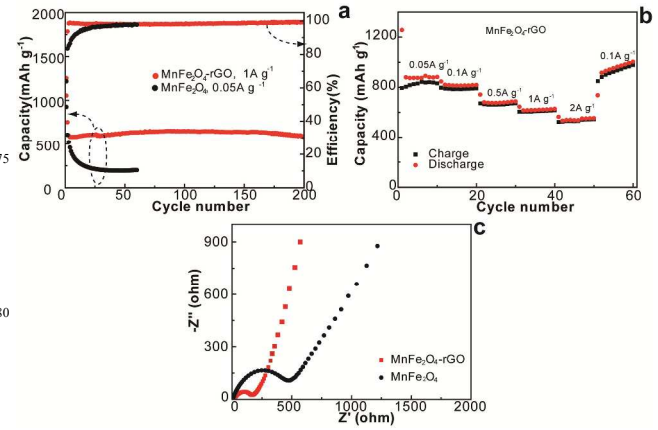

Figure 5. Electrochemical performances of $MnFe_2O_4$-rGO nanocomposite: (a) Cyclic stability for $MnFe_2O_4$–rGO nanocomposite at 1 A g^{-1} and that of $MnFe_2O_4$ at 0.05 A g^{-1}. Rate capability (b) and Nyquist plots (c) of $MnFe_2O_4$-rGO nanocomposite and bare $MnFe_2O_4$ nanoparticle right after the fifth charge process, respectively.

exhibited capacities of 1256.5 and 794 mAh g^{-1} for the discharge and charge cycles, respectively. The discharge capacity of 1256.5 mAh g^{-1} was much larger than the theoretical value of $MnFe_2O_4$-rGO nanocomposites ($C_{theoretical} = C_{MnFe2O4}$ × mass percentage of $MnFe_2O_4$ + C_{rGO} × mass percentage of rGO =930 × 80% + 372 × 20% = 818.4 mAh g^{-1}) (Note: though the initial capacity of graphene was high, its capacity dropped to the range of 200-300 mAh g^{-1} after several cycles.[6, 19]). The irreversible capacity loss in the initial cycle may be due to the irreversible reactions and the formation of a solid-electrolyte interface (SEI) layer on the electrode surface. Fig. 4b showed plots of differential capacity (dQ/dV) versus voltage during the first three cycles based on the discharge/charge profiles. In the first cycle, the main cathodic peak at 0.78 V had been associated with the reaction: $MnFe_2O_4 + 8Li^+ + 8e^- \rightarrow Mn^0 + 2Fe^0 + 4Li_2O$.[20] EIS measurements on $MnFe_2O_4$-rGO electrode right before cycling and after the first discharge process were also conducted. The result was shown in Fig. S4. After the discharge, additional semicircle appeared, which was due to the formation of SEI film. However, the diameter of semicircle corresponding the charge transfer resistance became smaller. It could be attributed to the reduction of Fe and Mn in $MnFe_2O_4$ into metallic state after the discharge.

This cathodic peak was positively shifted to 0.83 V in the second and subsequent cycle because of the polarization of electrode materials and the activation of the active materials.[21] The weak cathodic peak at 1.63 V may be due to the lithium interactions with the residual oxygen-containing functional groups within rGO.[22] Such peak was not observed in the subsequent cycles. The broad anodic peak near the same location was ascribed to the oxidation of metallic iron and manganese. After the first cycle, the dQ/dV curves of the $MnFe_2O_4$-rGO nanocomposite in the subsequent two cycles almost overlapped, revealing excellent reversibility. $MnFe_2O_4$-rGO nanocomposite exhibited superior cycling performance (Fig. 5a) than the bare $MnFe_2O_4$ nanoparticle. The capacities of the $MnFe_2O_4$-rGO nanocomposite were about 1055, 750.9, 584.6, 648.2 and 581.2 mAh g^{-1} in the 1st, 2nd, 10th, 100th and 200th cycle, respectively. In the third cycle, the Coulombic efficiency increased from 65.8% to 98.5%. After 200 cycles, the $MnFe_2O_4$–rGO electrode retained about 70% of the theoretical capacity at 1 A g^{-1}. However, even at a much smaller specific current of 0.05 A g^{-1}, the bare $MnFe_2O_4$ nanoparticle only kept capacities of 925.9, 604.8, 305.4 and 196 mAh g^{-1} in the 1st, 2nd, 10th and 50th cycle, respectively. The rate capability of the $MnFe_2O_4$-rGO nanocomposite at various discharge rates was revealed in Fig. 5b. Reversible capacities of 882.8, 819.3, 687.8, 628.1 and 554.5 mA h g^{-1} were achieved at discharge rates of 50, 100, 500, 1000 and 2000 mA g^{-1}, respectively. These values are 2.4, 2.2, 1.8, 1.7 and 1.5 times than the theoretical capacity of graphite (372 mAh g^{-1}), respectively. The electrochemical performance (cycling performance and rate capability) of our nanocomposite outperformed a lot of other nanocomposites, which were also summarized in Table S1. The extraordinary electrochemical performance relied on smaller $MnFe_2O_4$ nanoparticles well dispersed on graphene nanosheets compared with those reported in other work. Such morphology guaranteed the large quantity of accessible sites in the nanocomposite for fast Li^+ insertion/extraction and uniform dispersity in the nano scale for improved reversibility of the electrochemical reactions. More importantly, the improved electrochemical properties of nanocomposite could be attributed to wiring effect of rGO, that is, the unagglomerated large-sized rGO sheets could build an excellent conductive network which intimately contacted with $MnFe_2O_4$ nanoparticles and conductive carbon black, facilitating the electron transfer in the nanocomposite. This was further supported by electrochemical impedance spectroscopy (EIS) analyses performed on the nanocomposite and bare nanoparticle after the fifth charge process, respectively. Both Nyquist plots (Fig. 5c) consisted of one semicircle in the medium-frequency region and an inclined line in the low-frequency region, which could be related to charge-transfer resistance and the diffusion process of Li ions, respectively.[23] The diameter of the semicircle of $MnFe_2O_4$-rGO electrode was much smaller than that of $MnFe_2O_4$ electrode, indicating the enhanced electron conductivity of the $MnFe_2O_4$-rGO. While its inclined line exhibited larger slope than the bare $MnFe_2O_4$ nanoparticles, revealing better Li^+ diffusivity. Above results indicated that the conductive rGO sheets and the morphology of the synthesized nanocomposite significantly contributed to the cyclic stability and rate capability of the obtained composite.

Conclusions

In summary, $MnFe_2O_4$-rGO nanocomposite was successfully synthesized through a facile one-pot process. The as-synthesized $MnFe_2O_4$ nanoparticles had an average size of 10.0 nm, and anchored on the disordered rGO sheets. The obtained nanocomposite exhibited high reversible capacity, good rate capability and long cycle life. Even after 200 cycles at 1 A g^{-1}, its specific capacity retained 581.2 mAh g^{-1}, which was about 70% of the theoretical capacity. The excellent electrochemical performance was ascribed to wring effect of unagglomerated graphene and its intimate contact with well-dispersed small $MnFe_2O_4$ nanoparticles, which would prevent the aggregation of $MnFe_2O_4$ and guarantee the quick lithium-ion diffusion. The $MnFe_2O_4$-rGO nanocomposite could be a potential environmentally-benign high-capacity anode material for lithium ion batteries. The process we adopted here can provide a new economical and facile way to obtain the manganese–containing oxide and graphene composite for many applications.

Acknowledgment

This work was supported by the Scientific Research Foundation for Returned Scholars, the Ministry of Education of China, Key Basic Research Projects of Science and Technology Commission of Shanghai (No. 11JC1412900), and the National Science Foundation of China program (No. 21271140) and Jiangsu Environmental Protection Project (No. 2012005). Thank Dr. Zhong Shi for help on XRD and VSM.

Notes and references

[a] *Shanghai Key Laboratory of Special Artificial Microstructure Materials and Technology, School of Physics Science and Engineering, Tongji University, 1239 Siping Road, Shanghai 200092, China. Tel: 86-21-65988060; E-mail: zbao@tongji.edu.cn*

[b] *School of Mathematics and Physics, Jiangsu University of Technology, 1801 Zhongwu Road, Changzhou 213001, China*

† Electronic Supplementary Information (ESI) available: Nitrogen adsorption-desorption isotherms, Raman spectra and TGA analysis for the sample. See DOI: 10.1039/b000000x/

[1] (a)B. Kang, G. Ceder, *Nature* **2009**, *458*, 190; (b)M. Armand, J.-M. Tarascon, *Nature* **2008**, *451*, 652; (c)X. Zhu, Y. Zhu, S. Murali, M. D. Stoller, R. S. Ruoff, *ACS Nano* **2011**, *5*, 3333; (d)N. S. Choi, Z. Chen, S. A. Freunberger, X. Ji, Y. K. Sun, K. Amine, G. Yushin, L. F. Nazar, J. Cho, P. G. Bruce, *Angew. Chem. Int. Edit.* **2012**, *51*, 9994; (e)V. Etacheri, R. Marom, R. Elazari, G. Salitra, D. Aurbach, *Energ. Environ. Sci.* **2011**, *4*, 3243.

[2] H. Buqa, D. Goers, M. Holzapfel, M. E. Spahr, P. Novák, *J. Eelctrochem. Soc.* **2005**, *152*, A474.

[3] (a)P. Poizot, S. Laruelle, S. Grugeon, L. Dupont, J. Tarascon, *Nature* **2000**, *407*, 496; (b)P. G. Bruce, B. Scrosati, J. M. Tarascon, *Angew. Chem. Int. Edit.* **2008**, *47*, 2930; (c)L. Xiao, Y. Yang, J. Yin, Q. Li, L. Zhang, *J. Power Sources* **2009**, *194*, 1089.

[4] J. Su, M. Cao, L. Ren, C. Hu, *J. Phys. Chem. C* **2011**, *115*, 14469.

[5] (a)J. Liang, W. Wei, D. Zhong, Q. Yang, L. Li, L. Guo, *ACS Appl. Mater. Inter.* **2012**, *4*, 454; (b)P. Lian, X. Zhu, H. Xiang, Z. Li, W. Yang, H. Wang, *Electrochim. Acta* **2010**, *56*, 834.

[6] S. Liu, K. Chen, Y. Fu, S. Yu, Z. Bao, *Appl. Surf. Sci.* **2012**, *258*, 5299.

[7] (a)H. Wang, L. Cui, Y. Yang, H. Sanchez Casalongue, J. T. Robinson, Y. Liang, Y. Cui, H. Dai, *J. Am. Chem. Soc.* **2010**, *132*,

13978; (b)G. Yu, L. Hu, M. Vosgueritchian, H. Wang, X. Xie, J. R. McDonough, X. Cui, Y. Cui, Z. Bao, *Nano Lett.* **2011**, *11*, 2905.
[8] (a)M. Zhang, M. Jia, Y. Jin, *Appl. Surf. Sci.* **2012**, *261*, 298; (b)G. Zhou, D.-W. Wang, F. Li, L. Zhang, N. Li, Z.-S. Wu, L. Wen, G. Q. Lu, H.-M. Cheng, *Chem. Mater.* **2010**, *22*, 5306.
[9] Y. Xiao, J. Zai, L. Tao, B. Li, Q. Han, C. Yu, X. Qian, *Phys. Chem. Chem. Phys.* **2013**, *15*, 3939.
[10]D. Wang, D. Choi, J. Li, Z. Yang, Z. Nie, R. Kou, D. Hu, C. Wang, L. V. Saraf, J. Zhang, *ACS Nano* **2009**, *3*, 907.
[11]C. Nethravathi, B. Viswanath, J. Michael, M. Rajamathi, *Carbon* **2012**, *50*, 4839.
[12]S. Paek, E. Yoo, I. Honma, *Nano Lett.* **2008**, *9*, 72.
[13](a)W. S. Hummers Jr, R. E. Offeman, *J. Am. Chem. Soc.* **1958**, *80*, 1339; (b)L. J. Cote, F. Kim, J. Huang, *J. Am. Chem. Soc.* **2008**, *131*, 1043.
[14]V. Chandra, J. Park, Y. Chun, J. W. Lee, I.-C. Hwang, K. S. Kim, *ACS Nano* **2010**, *4*, 3979.
[15]C. Zhang, X. Peng, Z. Guo, C. Cai, Z. Chen, D. Wexler, S. Li, H. Liu, *Carbon* **2012**, *50*, 1897.
[16]Z. Wu, W. Ren, L. Wen, L. Gao, J. Zhao, Z. Chen, G. Zhou, F. Li, H.-M. Cheng, *ACS Nano* **2010**, *4*, 3187.
[17]A. Ferrari, J. Meyer, V. Scardaci, C. Casiraghi, M. Lazzeri, F. Mauri, S. Piscanec, D. Jiang, K. Novoselov, S. Roth, *Phys. Rev. Lett.* **2006**, *97*, 187401.
[18]J. Chen, C. Sorensen, K. Klabunde, G. Hadjipanayis, E. Devlin, A. Kostikas, *Phys. Rev. B* **1996**, *54*, 9288.
[19]D. Pan, S. Wang, B. Zhao, M. Wu, H. Zhang, Y. Wang, Z. Jiao, *Chem. Mater.* **2009**, *21*, 3136.
[20]Z. Zhang, Y. Wang, Q. Tan, Z. Zhong, F. Su, *J. Colloid Interf. Sci.* **2013**, *398*, 185.
[21]Z. Wang, D. Luan, S. Madhavi, Y. Hu, X. W. D. Lou, *Energ. Environ. Sci.* **2012**, *5*, 5252.
[22]C. Wang, D. Li, C. O. Too, G. G. Wallace, *Chem. Mater.* **2009**, *21*, 2604.
[23](a)M. Rahman, J.-Z. Wang, N. H. Idris, Z. Chen, H. Liu, *Electrochim. Acta* **2010**, *56*, 693; (b)L. Su, Z. Zhou, M. Ren, *Chem. Commun.* **2010**, *46*, 2590.

Supplementary Information

One-pot low-temperature synthesis of $MnFe_2O_4$-graphene composite for lithium ion battery application

Huang Tang, Peibo Gao, An Xing, Shuang Tian, and Zhihao Bao *

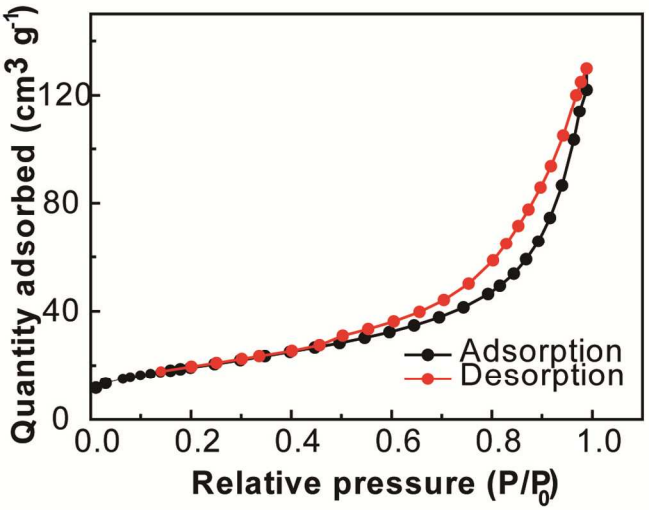

Figure S1. Nitrogen adsorption-desorption isotherms of $MnFe_2O_4$-rGO.

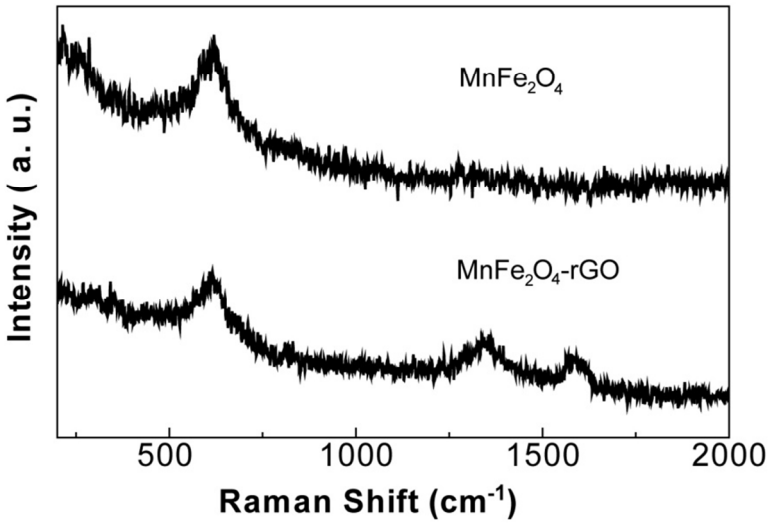

Figure S2. Raman spectra of $MnFe_2O_4$ and $MnFe_2O_4$-rGO.

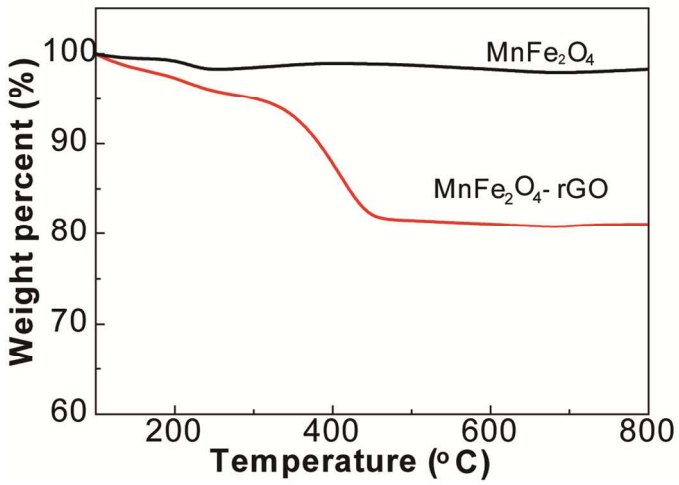

Figure S3. Thermogravimetric analyses of $MnFe_2O_4$ and $MnFe_2O_4$-rGO in air.

Table S1. Summary of synthesis process and electrochemical performance of transitional metal oxide-graphene nanocomponents reported in the literature.

No	Materials	Precursor	Preparation method	Current density ($A\ g^{-1}$)	Cycle number	Capacity ($mAh\ g^{-1}$)	Ref
1	Mn_3O_4-graphene	$Mn(Ac)_2$; purified graphene oxide	hydrothermal reaction at 180°C for 10 h	1.6	10	390	1
2	Graphene-Wrapped Fe_3O_4	$FeCl_3 \cdot 6H_2O$; graphene nanosheets	hydrolysis at 353 K for 24 h; heat-treated at 873K for 4 h	0.7	100	580	2
3	Fe_3O_4–graphene	$FeCl_3 \cdot 6H_2O$; purified graphene oxide	hydrothermal method at 180°C for 8 h	1.6	5	474	3
4	Fe_3O_4–graphene	$Fe(NO_3)_3 \cdot 9H_2O$; graphene sheets	gas/liquid interfacial reaction at 180 °C for 12 h	1.0	10	410	4
5	Fe_3O_4.reduced graphene oxide	$Fe_2(C_2O_4)_3 \cdot 5H_2O$; purified graphene oxide	hydrothermal reation at 180 °C for 10 h ; calcined at 500°C for 2 h	1.0	100	403	5
6	$MnFe_2O_4$–graphene	$MnCl_2$ and $FeCl_3 \cdot 6H_2O$; purified graphene oxide	hydrothermal reaction at 180 °C for 12 h for $MnFe_2O_4$, ultrasonication for 1.5 h for nanocomposite	1.0	90	767	6
7	$MnFe_2O_4$–graphene	$FeCl_3$; mixture directly from mixture by Hummer's method	low-temperature coprecipitation at 90°C for 4 h	1.0A	200	581.2	This work

1. H. Wang, L.-F. Cui, Y. Yang, H. Sanchez Casalongue, J. T. Robinson, Y. Liang, Y. Cui and H. Dai, Journal of the American Chemical Society, 2010, 132, 13978-13980.
2. G. Zhou, D.-W. Wang, F. Li, L. Zhang, N. Li, Z.-S. Wu, L. Wen, G. Q. Lu and H.-M. Cheng, Chemistry of Materials, 2010, 22, 5306-5313.
3. J. Su, M. Cao, L. Ren and C. Hu, The Journal of Physical Chemistry C, 2011, 115, 14469-14477.
4. P. Lian, X. Zhu, H. Xiang, Z. Li, W. Yang and H. Wang, Electrochimica Acta, 2010, 56, 834-840.
5. M. Zhang, M. Jia and Y. Jin, Applied Surface Science, 2012, 261, 298-305.
6. Y. Xiao, J. Zai, L. Tao, B. Li, Q. Han, C. Yu and X. Qian, Physical Chemistry Chemical Physics, 2013, 15, 3939-3945.

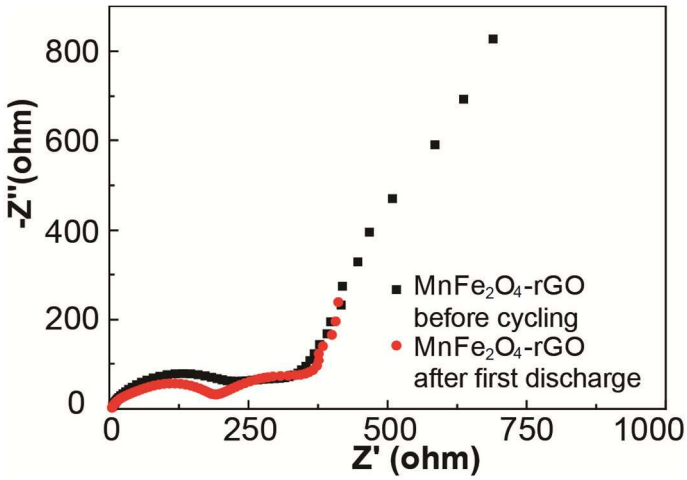

Figure. S4 Nyquist plots of $MnFe_2O_4$-rGO nanocomposite before and right after the first discharge process, respectively